



An investigation on machined surface quality and tool wear during creep feed grinding of powder metallurgy nickel-based superalloy FGH96 with alumina abrasive wheels

Ben-Kai Li¹ · Qing Miao¹ · Min Li¹ · Xi Zhang¹ · Wen-Feng Ding¹

Received: 4 October 2019 / Revised: 18 February 2020 / Accepted: 2 April 2020 / Published online: 30 April 2020
© Shanghai University and Springer-Verlag GmbH Germany, part of Springer Nature 2020

Abstract In this study, the machined surface quality of powder metallurgy nickel-based superalloy FGH96 (similar to Rene88DT) and the grinding characteristics of brown alumina (BA) and microcrystalline alumina (MA) abrasive wheels were comparatively analyzed during creep feed grinding. The influences of the grinding parameters (abrasive wheel speed, workpiece infeed speed, and depth of cut) on the grinding force, grinding temperature, surface roughness, surface morphology, tool wear, and grinding ratio were analyzed comprehensively. The experimental results showed that there was no significant difference in terms of the machined surface quality and grinding characteristics of FGH96 during grinding with the two types of abrasive wheels. This was mainly because the grinding advantages of the MA wheel were weakened for the difficult-to-cut FGH96 material. Moreover, both the BA and MA abrasive wheels exhibited severe tool wear in the form of wheel clogging and workpiece material adhesion. Finally, an analytical model for prediction of the grinding ratio was established by combining the tool wear volume, grinding force, and grinding length. The acceptable errors between the predicted and experimental grinding ratios (ranging from 0.6 to 1.8) were 7.56% and 6.31% for the BA and MA abrasive wheels, respectively. This model can be used to evaluate quantitatively the grinding performance of an alumina abrasive wheel, and is therefore helpful for

optimizing the grinding parameters in the creep feed grinding process.

Keywords Creep feed grinding · Powder metallurgy nickel-based superalloy · Surface quality · Alumina abrasive wheel · Tool wear

1 Introduction

Powder metallurgy nickel-based superalloy FGH96 (similar to Rene88DT) is a significant alternative engineering material for the manufacture of aero-engine turbine disks owing to its excellent properties of a superfine grain, homogeneous organization, high elevated temperature fatigue strength, and high yield strength [1]. However, it is also a typical difficult-to-cut material because it has low thermal conductivity and high strength like other nickel-based superalloy materials [2–6]. Abrasive wheel grinding is an important method for the machining of powder metallurgy nickel-based superalloy FGH96. However, in the grinding process, high grinding temperatures tend to occur, which can lead to a high risk of grinding burn and simultaneously induce mechanical and microstructural changes in the workpiece subsurface, including work hardening/thermal softening, white layers, micro-cracks, and phase transitions [7–10]. The low machinability of such nickel-based superalloys significantly increases the difficulty of obtaining a high quality machined surface [11].

Additionally, during grinding of superalloy FGH96, abrasive wheel wear can very easily occur [12], which can reduce the service life of the abrasive wheel. Moreover, with increasing abrasive wheel wear, the machined surface quality can significantly degrade. To solve these problems, further study of the machinability of the powder metallurgy

✉ Wen-Feng Ding
wfding@nuaa.edu.cn

¹ National Key Laboratory of Science and Technology on Helicopter Transmission, Nanjing University of Aeronautics and Astronautics, Nanjing 210016, People's Republic of China

nickel-based superalloy FGH96 during grinding is necessary to achieve the expected machined surface quality and improved machining efficiency.

In recent years, extensive research on the surface quality and grinding characteristics of nickel-based superalloys has been conducted. For instance, Zhou et al. [13] carried out grinding experiments on nickel-based single crystal superalloy DD98. The effects of abrasive wheel speed, workpiece infeed speed, and depth of cut on the machined surface roughness were studied. The results indicated that the abrasive wheel speed had the greatest impact on the surface roughness, followed by the workpiece infeed speed, while the depth of cut had the least impact on the surface roughness. Żyłka et al. [14] studied the impact of the abrasive wheel speed on the ground surface quality by grinding nickel-based wrought superalloy GH4169 (similar to Inconel718) with white alumina (WA) abrasive wheels. The surface roughness R_a was found to decrease with increasing abrasive wheel speed. Moreover, the ground surface roughness R_a value was reduced by approximately 30% with an increase in the abrasive wheel speed from 22 m/s to 25 m/s. However, as the degree of abrasive wheel wear increased, the surface roughness R_a increased markedly. Zeng et al. [15] investigated the surface integrity of GH4169 with a single alumina abrasive wheel under different grinding parameters. The results indicated that the depth of cut had the most significant effect on the machined surface roughness. When the depth of cut was increased from 5 μm to 40 μm , the surface roughness R_a increased by a factor of 3, from 0.3 μm to 0.9 μm . A vertical crack appeared on the workpiece surface with an increase in the material removal rate to 6.7 $\text{mm}^3/(\text{mm}\cdot\text{s})$. Workpiece surface defects have also been studied. For example, Miao et al. [16] conducted creep feed grinding experiments on the abrasive wheel wear of nickel-based wrought superalloy GH4169, directional casting superalloy DZ408, and single crystal DD6 superalloy using microcrystalline alumina (MA) and brown alumina (BA) abrasive wheels. The results indicated that the surface defect morphology (such as smeared workpiece material and scratches) produced by the BA abrasive wheel was not parallel to the grinding direction mainly because of the fall-out and fracture of the abrasive particles. In contrast, the defects of the grooves occurred on the workpiece surface along the grinding direction for the MA abrasive wheel. The reasons were the high hardness and ductility of the abrasive particles. Li et al. [17] analyzed the effects of the dressing parameters of abrasive wheels on the machined surface quality of GH4169. They found that the dresser feed speed had a distinct impact on the machined surface. In addition, the fewest defects such as material stacking and smearing were obtained when a dresser feed speed of 200 mm/min and

depth of dressing cut of 0.02 mm were selected. Furthermore, Qian et al. [18] comparatively analyzed the ground surface defects (including material smearing and chip redeposition) and surface roughness during grinding of wrought superalloy GH4169 and cast superalloy K4125 with a BA abrasive wheel. The results indicated that the surface defects of K4125 were greater than those of GH4169, and the surface roughness value of GH4169 was lower than that of K4125. Yao et al. [19] conducted a comparative experiment on the grinding of GH4169 with a single alumina abrasive wheel and resin cubic boron nitride (CBN) abrasive wheels. The results showed that the surface roughness R_a was 0.112 μm with grinding parameters of $a_p = 0.005$ mm, $v_w = 16$ m/min, and $v_s = 25$ m/s using the single alumina abrasive wheel. Wang et al. [20] conducted minimum quantity lubrication (MQL) grinding experiments on GH4169 with different nanofluids using a white alumina abrasive wheel. It was found that the highest grinding ratio, lowest friction coefficient, and lowest surface roughness were obtained during grinding with an alumina nanofluid. Xu et al. [21] conducted an experimental investigation of the grinding temperature during the grinding of cast superalloy K417 using a white alumina abrasive wheel. The surface quality was studied. Grinding thermal damage was found when the grinding temperature reached a critical value. With increasing grinding temperature, the surface quality deteriorated, and the surface roughness increased. In addition, Sinha et al. [22] studied grinding burn during the grinding of GH4169 with a white alumina abrasive wheel and a silicon carbide (SiC) abrasive wheel. The results indicated that SiC abrasive wheel grinding was more likely to cause surface burning, and the roughness of the burned surface was 10% higher than the unburned surface. Moreover, they found that abrasive wheel wear played a significant part in the surface burning of the workpiece. Naskar et al. [23] conducted a grinding experiment with Inconel 718 using CBN abrasive wheels and compared the machined surface quality obtained under different lubrication conditions. The best surface roughness was obtained with pure-oil MQL grinding. Ding et al. [24] studied the surface quality during creep feed experimental grinding of K424 cast superalloy with a CBN abrasive wheel. The results showed that the grinding temperature was effectively controlled at approximately 100 $^\circ\text{C}$, although the specific grinding energy reached 200–300 J/mm^3 . Good surface quality was obtained, while burns and cracks were not observed on the surface of the workpiece.

The above literature has reported extensive research on the surface quality and grinding characteristics of superalloy materials under various machining conditions. However, these studies have rarely involved powder metallurgy superalloy materials. Thus, it is necessary to research the machinability of the FGH96 material.

Moreover, alumina abrasive wheels with large pores are widely used in practice to grind difficult-to-cut materials like superalloys owing to their easy dressing operation and low cost. Therefore, in the present study, BA and MA abrasive wheels were used to creep feed grind the powder metallurgy nickel-based superalloy FGH96. The machined surface quality and grinding characteristics including the grinding force, grinding temperature, and tool wear behavior were analyzed comparatively under different combinations of grinding parameters. In addition, an analytical model for prediction of the grinding ratio was established. The results can provide guidance for further improving the grinding process for the FGH96 material.

2 Experimental details

The workpiece material was powder metallurgy superalloy FGH96, with dimensions of 25 mm × 25 mm × 5 mm. The chemical composition and mechanical properties of FGH96 are listed in Tables 1 and 2, respectively. According to Table 2, the FGH96 material could still maintain high strength at high temperatures. For example, its tensile strength and yield strength at 750 °C could reach 1 260 MPa and 1 030 MPa, respectively. Surface grinding experiments were conducted with BA and MA abrasive wheels (400 × 20 × 127-80F6V45, Sisha Co., Ltd. China). The size of 80# abrasive grains is approximately 150–180 μm. The Vickers hardness and fracture toughness of the BA abrasive wheel are 20.3 GPa and 2.7 MPa·m^{1/2}, respectively, and they are 21.5 GPa and 3.9 MPa·m^{1/2} for the MA abrasive wheel, respectively [16, 25]. The surface morphologies of the two types of abrasive wheels are shown in Fig. 1.

The grinding experiments were conducted on a surface grinder with high speed (model BLOHM PROFIMAT MT-408) having a maximum output power and spindle speed of 45 kW and 8 000 r/min, respectively. The precision of the grinder was 1 μm. The experimental setup and conditions for the grinding process are shown in Fig. 2 and Table 3, respectively, in which the creep feed grinding parameters were used [26]. The wheel dressing was performed by a single diamond and the dressing parameters were as follows: the total depth of dressing was 0.2 mm; the depth of the dressing cut was 0.02 mm; and the dresser feed speed was 200 mm/min. In general, this parameter combination could ensure good grinding performance of the BA and

MA alumina wheels based on pre-experiment results in Ref. [17].

A 3-channel piezoelectric dynamometer (KISTLER 9317C) together with a charge amplifier (KISTLER 5018) and semi-natural thermocouple were utilized to monitor the grinding force and temperature, respectively. Sampling frequencies of 5 kHz, 5 kHz and 20 kHz, were set for the *x*, *y*, and *z* directions of the dynamometer, respectively. It is generally believed that the grinding force is composed of normal and tangential grinding forces during a surface grinding process without axial feeding. Thus, the *x* and *z* directions of the dynamometer were exploited to monitor the tangential and normal grinding forces, respectively. The components of the semi-natural thermocouple are shown in Fig. 2. The grinding temperature was computed using Eq. (1). The role of the mica plate was to isolate the workpiece and the constantan wire. The sealant was used to prevent the grinding fluid from damaging the thermocouple during grinding, and the wire was connected to the signal collector to record the temperature signal data. The machined surface roughness was analyzed by a surface roughness tester (Mahr M1) and the ground surface was measured by Sensofar S Neox 3D confocal microscopy. The setting parameters were a tip diameter of 0.2 μm, a Gaussian filter for the filtering, and a setting cut of 0.8 mm. The experimental results were averaged based on five measured values. In addition, the abrasive wheel was dressed according to the given parameters after every test. The surface morphology of the workpiece and the abrasive wheel were examined using a KH-7700 optical microscope and a Quanta 200 scanning electron microscope.

$$T_{\text{FGH96}} = -0.0367u^2 + 12.395u + 25.968, \quad (1)$$

where T_{FGH96} is the grinding temperature of the workpiece material and u is the measured thermal electromotive force.

3 Results and discussion

3.1 Grinding force analysis

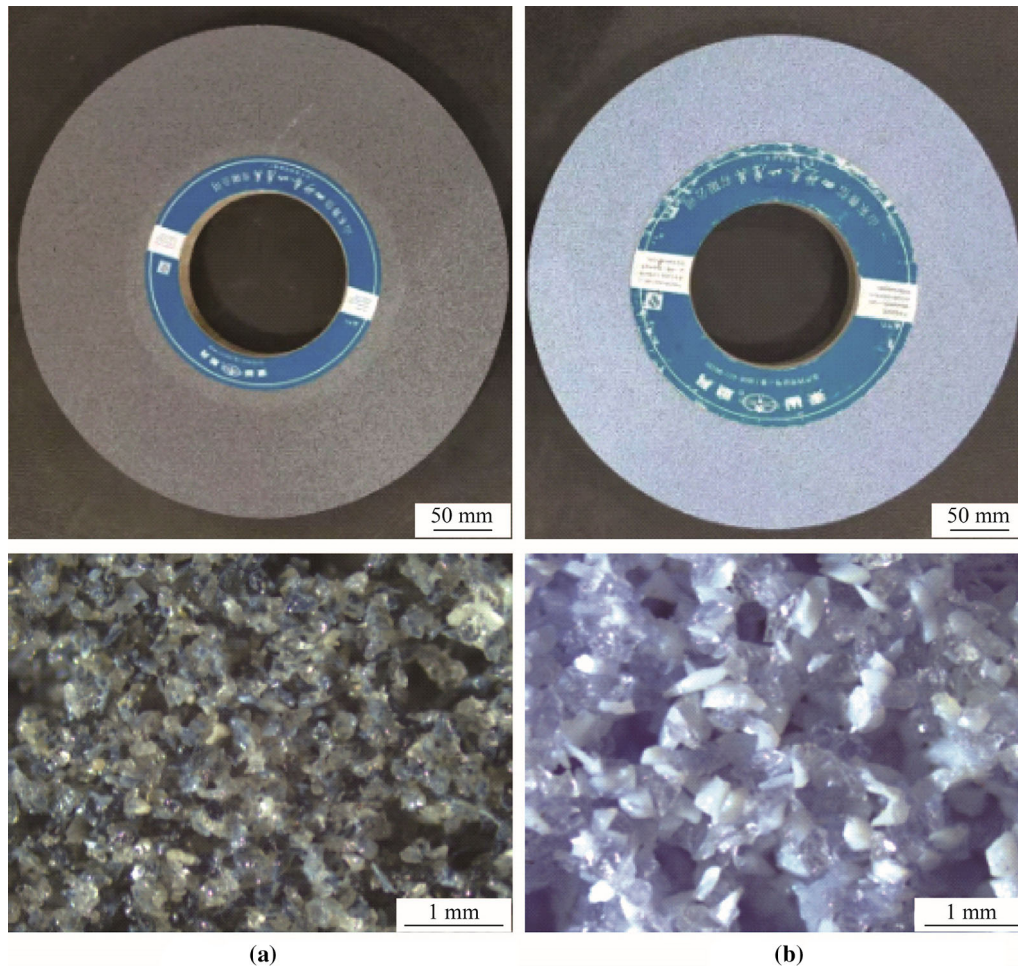
The grinding force, which has an important influence on tool wear and machined surface quality [27, 28], can be used to estimate the grinding features of materials. Figure 3 shows a comparison of the specific grinding force between the BA abrasive wheel and MA abrasive wheel. Although the grinding forces of the BA abrasive wheel are slightly

Table 1 Chemical composition of FGH96 material

Element	Co	Cr	Mo	W	Al	Ti	Nb	B	Zr	C	Ni	Mn	Cu	Fe
Content (mass fraction, %)	13	16	4	4	2.2	3.7	0.8	0.01	0.04	0.04	Bal.	–	–	0.1

Table 2 Mechanical properties of FGH96 material at 20 °C and 750 °C

Materials	Temperature/°C	Tensile strength σ_b /MPa	Yield strength $\sigma_{0.2}$ /MPa	Density ρ /(kg·m ⁻³)	Thermal conductivity k /(W·(m·K) ⁻¹)
FGH96	20	1 520	1 200	8 255	9.5
	750	1 260	1 030	–	–

**Fig. 1** Surface morphology of **a** BA abrasive wheel and **b** MA abrasive wheel

higher than those of the MA abrasive wheel, the tangential grinding force and normal grinding force of both types of abrasive wheels are generally very close. In Fig. 3a, as the depth of cut gradually increases from 0.2 mm to 1.0 mm, both the tangential grinding force and normal grinding force exhibit an increasing trend. For instance, the tangential forces of the BA and MA abrasive wheels increase from 5.39 and 5.31 N/mm to 10.47 and 9.8 N/mm, respectively, and the normal force increases from 17.17 and 17.13 N/mm to 41.41 and 41.0 N/mm, respectively. According to Fig. 3b, both the tangential force and normal force also exhibit a slightly increasing trend as the workpiece infeed speed gradually increases from 80 mm/min to

200 mm/min. The normal grinding forces of the BA abrasive wheel and the MA abrasive wheel increase from 26.37 and 26 N/mm to 35.63 and 33.5 N/mm, respectively, and the tangential grinding forces increase from 7.3 and 7.67 N/mm to 8.91 and 9.67 N/mm, respectively. With increasing abrasive wheel speed from 20 m/s to 35 m/s, a decreasing trend was observed in the tangential grinding force, as seen in Fig. 3c. The tangential grinding forces of the BA and MA abrasive wheels decrease from 8.72 and 9.18 N/mm to 6.72 and 6.64 N/mm, respectively, but the change in the normal grinding force is not obvious, and a slightly decreasing trend is also observed. The normal grinding forces of both the BA abrasive wheel and MA

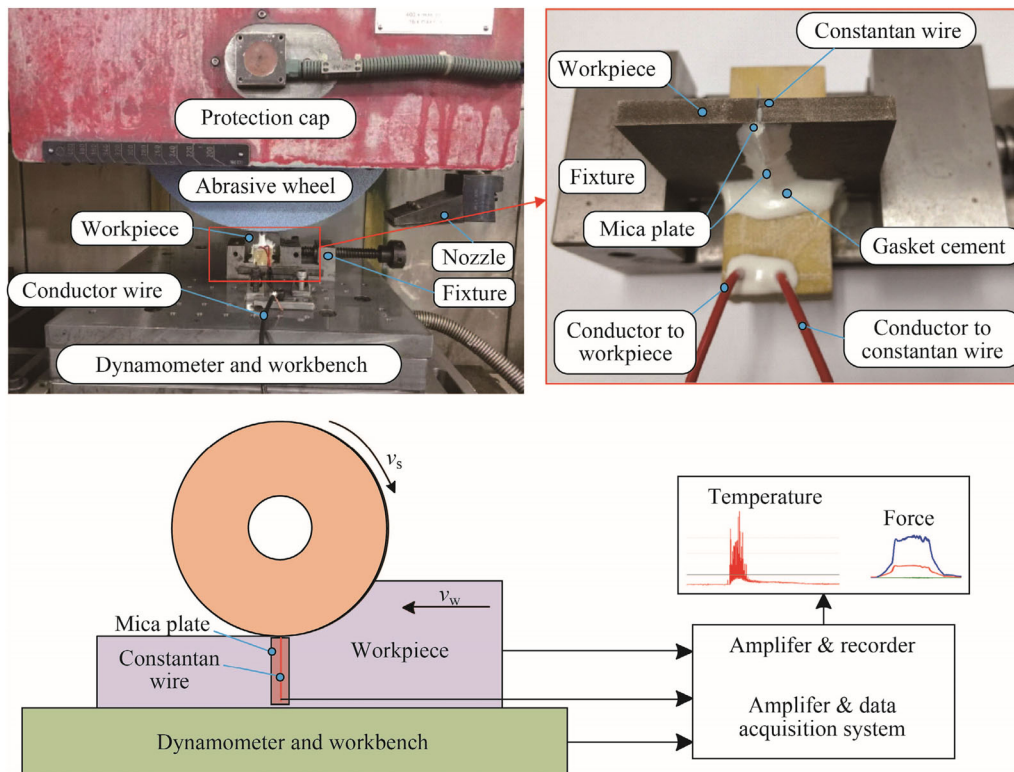


Fig. 2 Experimental setup and measuring sketch map

Table 3 Grinding conditions

Conditions	Parameters	Conditions	Parameters
Grinding mode	Down-grinding	Grinding width of workpiece, b_w /mm	5
Abrasive wheel speed, v_s /(m·s ⁻¹)	20, 25, 30, 35	Cooling lubricant	5% emulsified dilution liquid
Workpiece infeed speed, v_w /(mm·min ⁻¹)	80, 100, 120, 150, 180, 200	Flow rate/(L·min ⁻¹)	90
Depth of cut, a_p /mm	0.2, 0.5, 0.6, 0.7, 1.0	Flow pressure/MPa	1.5

abrasive wheel are maintained at approximately 31.0 N/mm. According to Fig. 3d, with increasing material remove rate, the tangential grinding force of the two types of abrasive wheels shows a gradually increasing trend.

3.2 Grinding temperature analysis

Grinding is a process that removes material with a negative rake angle of the abrasive grains. Accordingly, most of the energy consumed during grinding is converted into heat, which accumulates within the grinding zone to cause a temperature rise [29–31] and can adversely affect the machined surface quality. For example, when the grinding temperature exceeds the critical value, the machined surface of the workpiece will be burned and the fatigue life of the finished parts will be reduced [32]. The measured

values were the thermal electromotive force of the grinding zone, as shown in Fig. 4. The temperature was computed using Eq. (1). A comparison of the grinding temperature results during the grinding of FGH96 using two types of abrasive wheels is shown in Fig. 5. It can be found that the grinding temperatures of the two types of abrasive wheels are very close. The grinding temperature of the MA abrasive wheel is slightly lower than that of the BA abrasive wheel. With increasing depth of cut, as shown in Fig. 5a, a gradually increasing trend was observed in the grinding temperature. The grinding temperatures of the BA abrasive wheel and MA abrasive wheel increase from 84.4 °C to 91.2 °C and from 83.6 °C to 90.0 °C, respectively, with increasing depth of cut from 0.2 mm to 0.7 mm. From the aspect of the coolant, this is related to the nuclear cooling of the grinding fluid during creep feed deep grinding

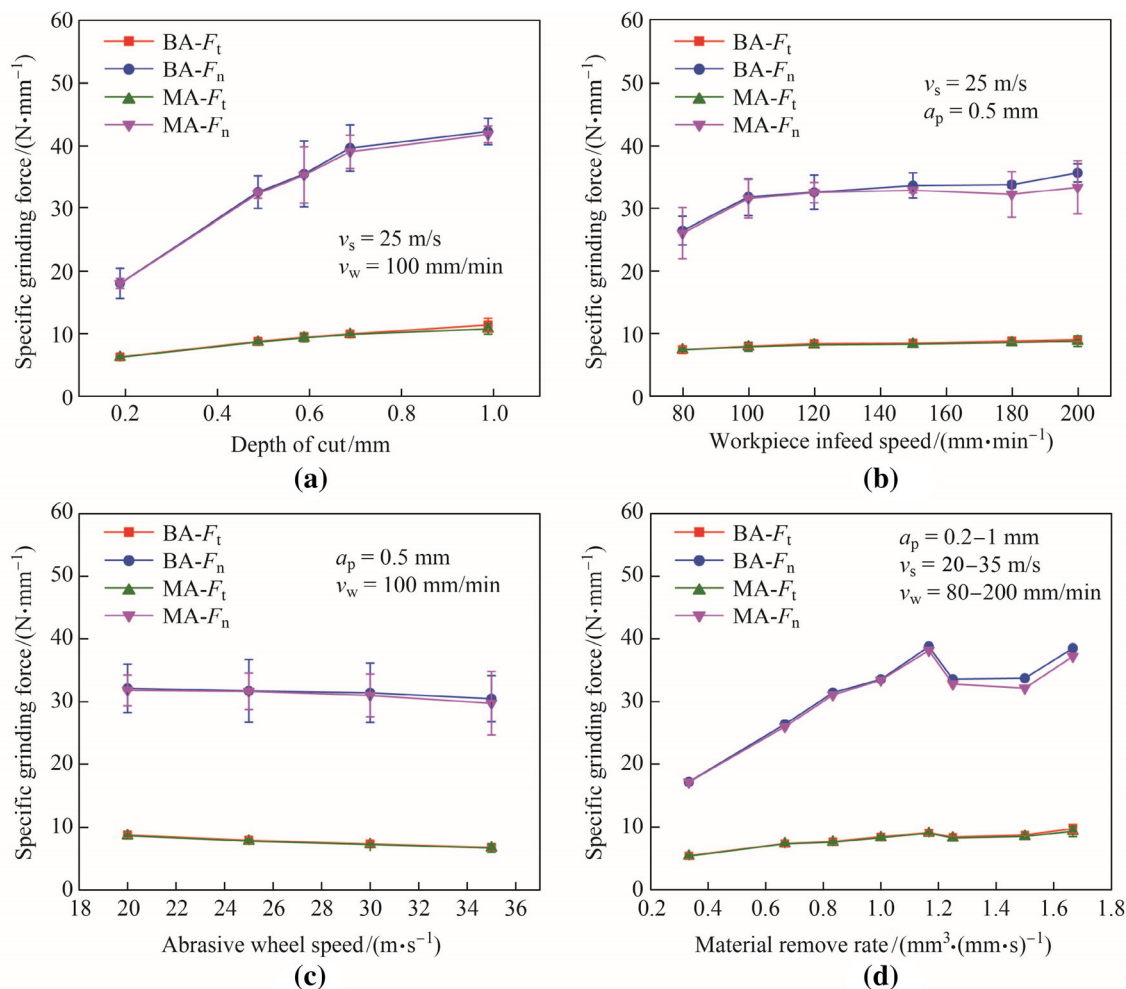


Fig. 3 Effects of **a** depth of cut, **b** workpiece infeed speed, **c** abrasive wheel speed and **d** material remove rate on specific grinding force (the tangential force F_t , normal grinding force F_n)

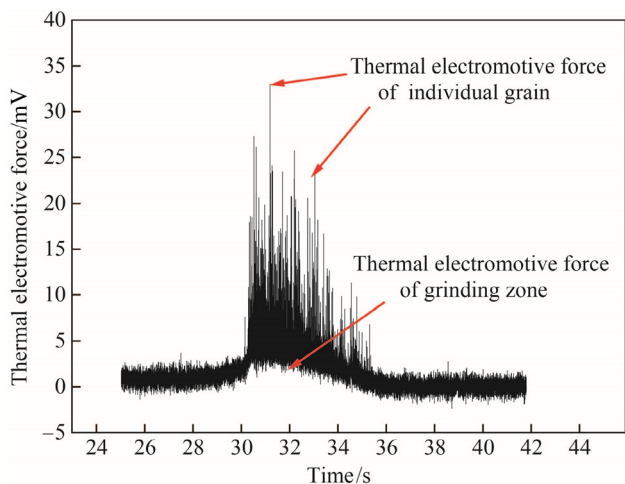


Fig. 4 Measured typical grinding temperature signal

[33, 34]. However, when a_p is 1.0 mm (the material removal rate is 1.67 mm³/(mm·s), the grinding temperature increases sharply to more than 700 °C, leading to a

detrimental influence on the machined surface quality. As shown in Fig. 5b, as the workpiece infeed speed increases from 80 mm/min to 200 mm/min, the grinding temperature of the two types of abrasive wheels exhibit an increasing trend. When the workpiece infeed speed increases from 80 mm/min to 180 mm/min, the grinding temperatures of the BA and MA abrasive wheels gradually increase from 81.5 °C to 99.0 °C and from 80.1 °C to 97.5 °C, respectively. When v_w is 200 mm/min, the grinding temperatures of the MA abrasive wheel and BA abrasive wheel are 103.9 °C and 583.0 °C, respectively. This is due to the deterioration of the grinding conditions when the workpiece infeed speed is set as 200 mm/min using the BA abrasive wheel [35]. As a result, the generated heat rapidly increases and exceeds the cooling capacity of the grinding liquid. At this time, the cooling state within the workpiece-tool grinding zone is changed from the nuclear state into film-forming boiling, which leads to a rapidly increasing temperature of the grinding zone [36]. In contrast, the wear resistance of the MA abrasive wheel is better than that of

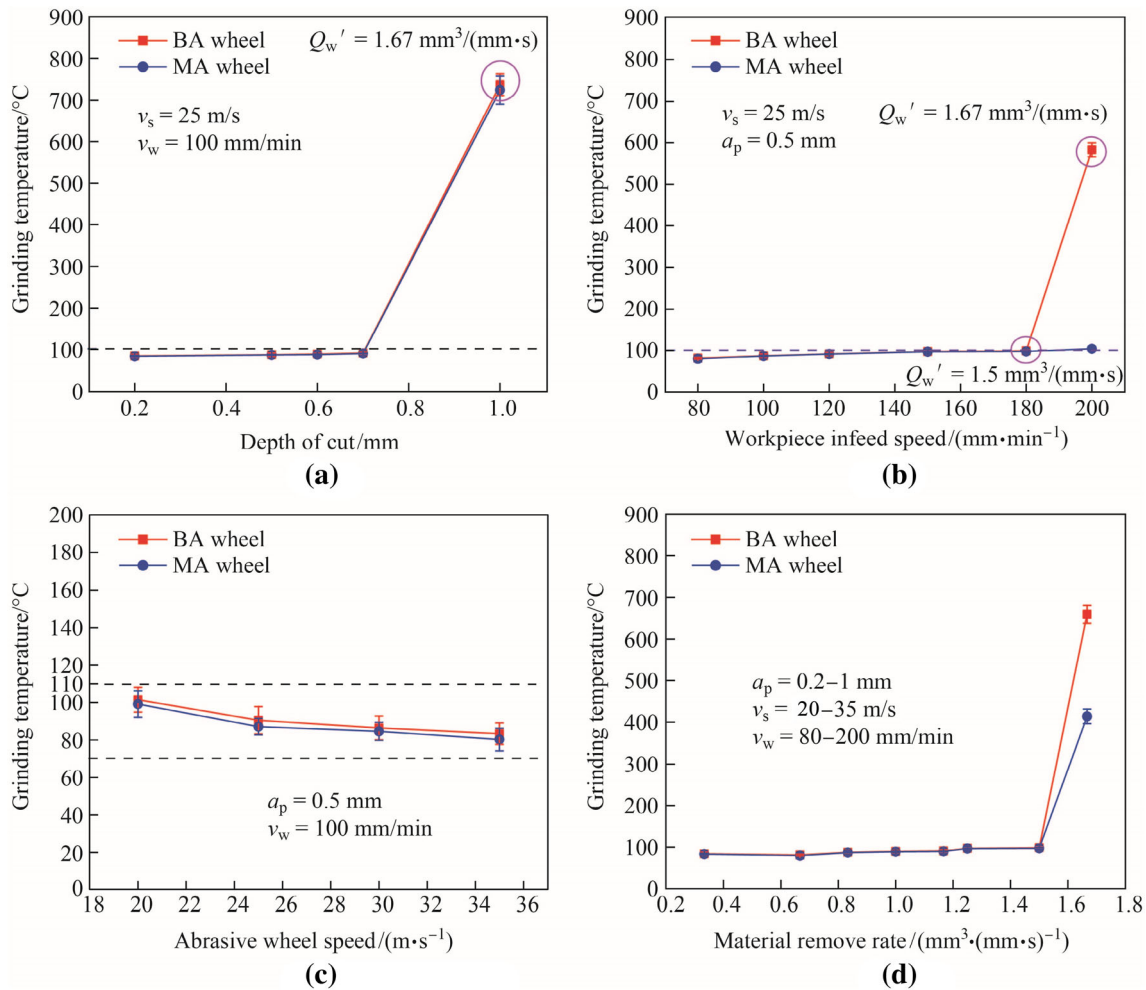


Fig. 5 Effects of **a** depth of cut, **b** workpiece infeed speed, **c** abrasive wheel speed and **d** material remove rate on grinding temperature

the BA abrasive wheel. At the same material removal rates, the MA abrasive wheel can maintain sharpness as a result of its self-sharpening behavior, and thus less heat is generated in the grinding zone. Therefore, the grinding fluid could still transfer the grinding heat through the nuclear boiling process, thereby ensuring a low grinding temperature. It can be seen from Fig. 5c that the grinding temperature is gradually reduced as the abrasive wheel speed increases and is maintained between 70 °C and 110 °C owing to the nuclear boiling heat transfer of the coolant according to the theory of normal creep-fed deep grinding [37]. As shown from Fig. 5d, based on the experimental results for the grinding temperature, the maximum material removal rates (Q_w') of the BA and MA abrasive wheels without grinding burn are 1.5 mm³/(mm·s) and 1.6 mm³/(mm·s), respectively. This indicates that the MA abrasive wheel has a slightly higher grinding efficiency compared to the BA abrasive wheel.

3.3 Ground surface analysis

The grinding surface roughness and surface topography such as marks or defects are generally the most significant parameters for estimating the grinding surface quality [38–41]. Figure 6 shows the cross-sectional profiles obtained using the two types of abrasive wheels in the case of $a_p = 0.5 \text{ mm}$, $v_s = 25 \text{ m/s}$, and $v_w = 100 \text{ mm/min}$. The surface roughness values were measured at multiple positions perpendicular to the grinding direction. As shown in Figs. 6a, b, the peak values for the groove height on the machined surface with BA and MA abrasive wheel are all $-2.0 \text{ }\mu\text{m}$ and $0.8 \text{ }\mu\text{m}$.

Figure 7 shows the experimental results for the ground surface roughness, which are generally similar for the two types of abrasive wheels. In Fig. 7a, as the depth of cut increases from 0.2 mm to 1.0 mm, the machined surface roughness values with the BA and MA abrasive wheels increase from 0.26 and 0.29 μm to 0.82 and 0.82 μm , respectively. It should be noted that when a_p is below

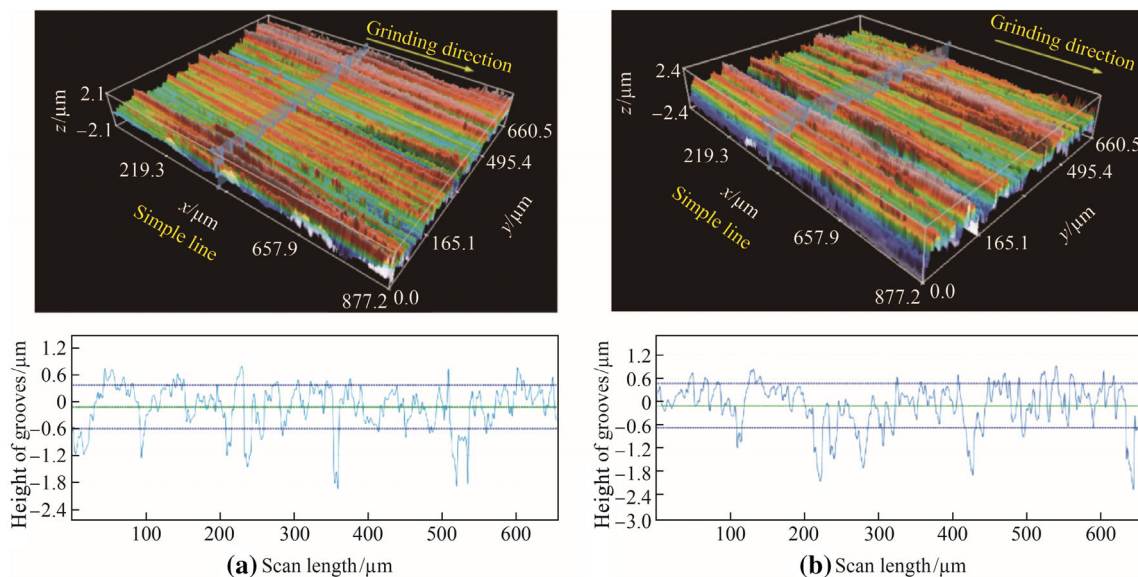


Fig. 6 Ground surface profile produced by a BA and b MA abrasive wheels

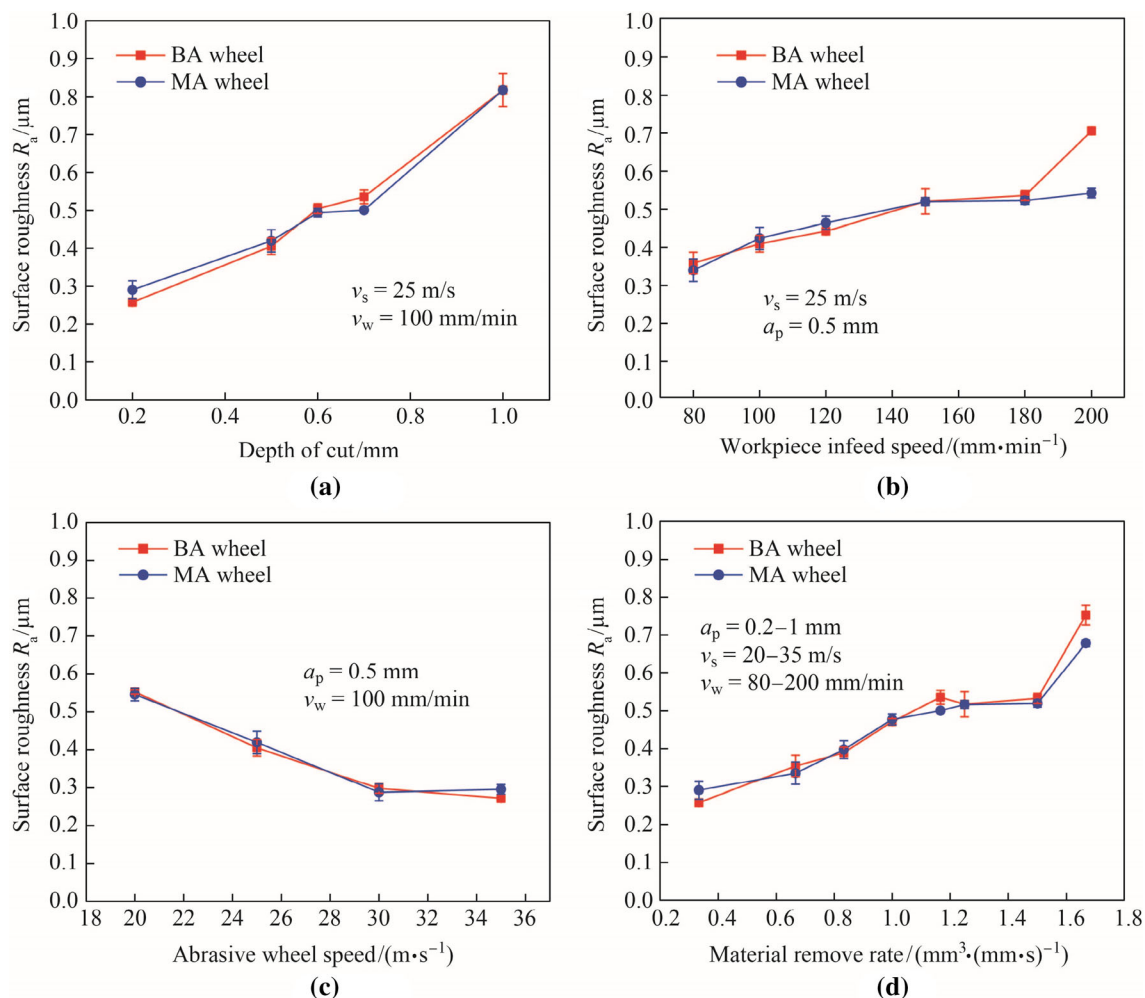


Fig. 7 Effects of a depth of cut, b workpiece infeed speed, c abrasive wheel speed and d material remove rate on surface roughness

1.0 mm, the machined surface roughness R_a with both the BA and MA abrasive wheels is less than $0.8 \mu\text{m}$, while when a_p is 1 mm, the ground surface roughness R_a is more than $0.8 \mu\text{m}$. This is mainly due to the adverse effect of the grinding temperature on the machined surface. As shown in Fig. 7b, with increasing workpiece infeed speed from 80 mm/min to 200 mm/min, the surface roughness tends to increase, showing that the ground surface roughness with the BA abrasive wheel and MA abrasive wheel increases from 0.35 and $0.34 \mu\text{m}$ to 0.7 and $0.53 \mu\text{m}$, respectively. As the abrasive wheel speed increases from 20 m/s to 35 m/s, the machined surface roughness values with the BA abrasive wheel and MA abrasive wheel are less than $0.6 \mu\text{m}$, and the surface roughness values gradually decrease from $0.55 \mu\text{m}$ to $0.27 \mu\text{m}$ and from $0.55 \mu\text{m}$ to $0.3 \mu\text{m}$, respectively, as shown in Fig. 7c. With increasing material removal rate, the surface roughness of the ground workpiece tends to increase, as shown in Fig. 7d.

Figure 8 shows the typical surface morphology and surface defects during grinding of the FGH96 material by two types of abrasive wheels. Under the conditions of $v_s = 25 \text{ m/s}$, $v_w = 200 \text{ mm/min}$, and $a_p = 0.5 \text{ mm}$, the workpiece surface morphology obtained with MA abrasive wheel grinding is obviously better than that obtained with the BA abrasive wheel, as shown in Figs. 8a, b. Under the current experimental conditions, this is mainly due to the high grinding temperature during the BA abrasive wheel grinding, which leads to smearing of the workpiece material. Moreover, when the grinding parameters are $v_s = 25 \text{ m/s}$, $v_w = 100 \text{ mm/min}$, and $a_p = 0.5 \text{ mm}$ and 0.7 mm , there is no obvious difference between the ground surfaces obtained with the BA abrasive wheel and MA abrasive wheel, as shown in Figs. 8e–h. However, the furrows on the machined surface produced by the MA abrasive wheel grinding are shallower than those from the BA abrasive wheel at $v_s = 30 \text{ m/s}$, $v_w = 100 \text{ mm/min}$, and $a_p = 0.5 \text{ mm}$, as shown in Figs. 8c, d.

Ground surface defects on a workpiece will inevitably appear during the grinding process owing to the influence of the machining conditions and the properties of the workpiece material. Defect formation is strongly controlled by the tool wear behavior [16]. For instance, workpiece surface scratches, as shown in Fig. 8e, are mainly caused by the slippage of crushed or broken abrasive grain particles. At the same time, deep grooves appear on the workpiece surface, as shown in Fig. 8h. These are formed when the crushed or broken abrasive particles are pressed into the material matrix and then skid. In addition, material that is not removed from the grinding zone in time and has large plastic deformation and material that has adhered to the abrasive wheel surface can cause workpiece surface smearing, as shown in Fig. 8f. Furthermore, voids in the workpiece surface are observed, as shown in Fig. 8g; these

may be introduced by the preparation process of the FGH96 material. The generation of machined surface micro-cracks is mainly caused by the release of residual stress after grinding [42, 43]. However, further research is required to establish the specific causes.

3.4 Tool wear analysis

The wear behavior can reflect the wear-resisting ability of an abrasive wheel to a certain extent, and it is an important factor affecting the ground surface quality. The radial wear of the abrasive wheels in the current study was measured by grinding a graphite block to duplicate the wear profile of the abrasive wheel. However, it is difficult to detect because the amount of wear on the abrasive wheel is very small after a single grinding stroke. In order to improve the measurement accuracy, the abrasive wheel was measured after five grinding strokes. As shown in Fig. 9, the vertical distance between the two parallel lines on the graphite block is the value of the abrasive wheel radial wear. The experimental results for the abrasive wheel radial wear per unit length (i.e., the ratio of radial wear to workpiece length) are shown in Fig. 10. The radial wear of the BA and MA abrasive wheels exhibits almost the same trends with the various grinding parameters. In addition, the radial wear of the MA abrasive wheel is slightly lower than that of the BA abrasive wheel because the hardness of the BA abrasive wheel is lower than that of the MA abrasive wheel. It can be seen that as the abrasive wheel speed, workpiece infeed speed, and depth of cut increase, the radial wear of the two types of abrasive wheels also tends to increase. Moreover, as shown in Fig. 10a, as the depth of cut increases from 0.2 mm to 1 mm, the radial wear of the BA and MA abrasive wheels increases from 0.24 and $0.23 \mu\text{m/mm}$ to 0.45 and $0.44 \mu\text{m/mm}$, respectively, which are both equivalent to an increase of approximately 87.5%. As the workpiece infeed speed increases from 80 mm/min to 200 mm/min, the BA and MA abrasive wheel radial wear increase from $0.25 \mu\text{m/mm}$ to 0.33 and $0.32 \mu\text{m/mm}$, respectively, equivalent to increases of 32% and 28%, as shown in Fig. 10b. As shown in Fig. 10c, with increasing abrasive wheel speed, the radial wear values for the BA abrasive wheel and MA abrasive wheel have similar ranges to those displayed in Fig. 10b. The increase percentage is up to 32%. This tendency may occur because the contact frequency of the tool and workpiece increased with an increase in the abrasive wheel speed from 20 m/s to 35 m/s. Moreover, as the material removal rate increases, the abrasive wheel wear exhibits an increasing trend, as shown in Fig. 10d.

The wear surface morphologies of the MA and BA abrasive wheels are shown in Fig. 11. Band-shaped chips clogging the pores of the abrasive wheels can be clearly

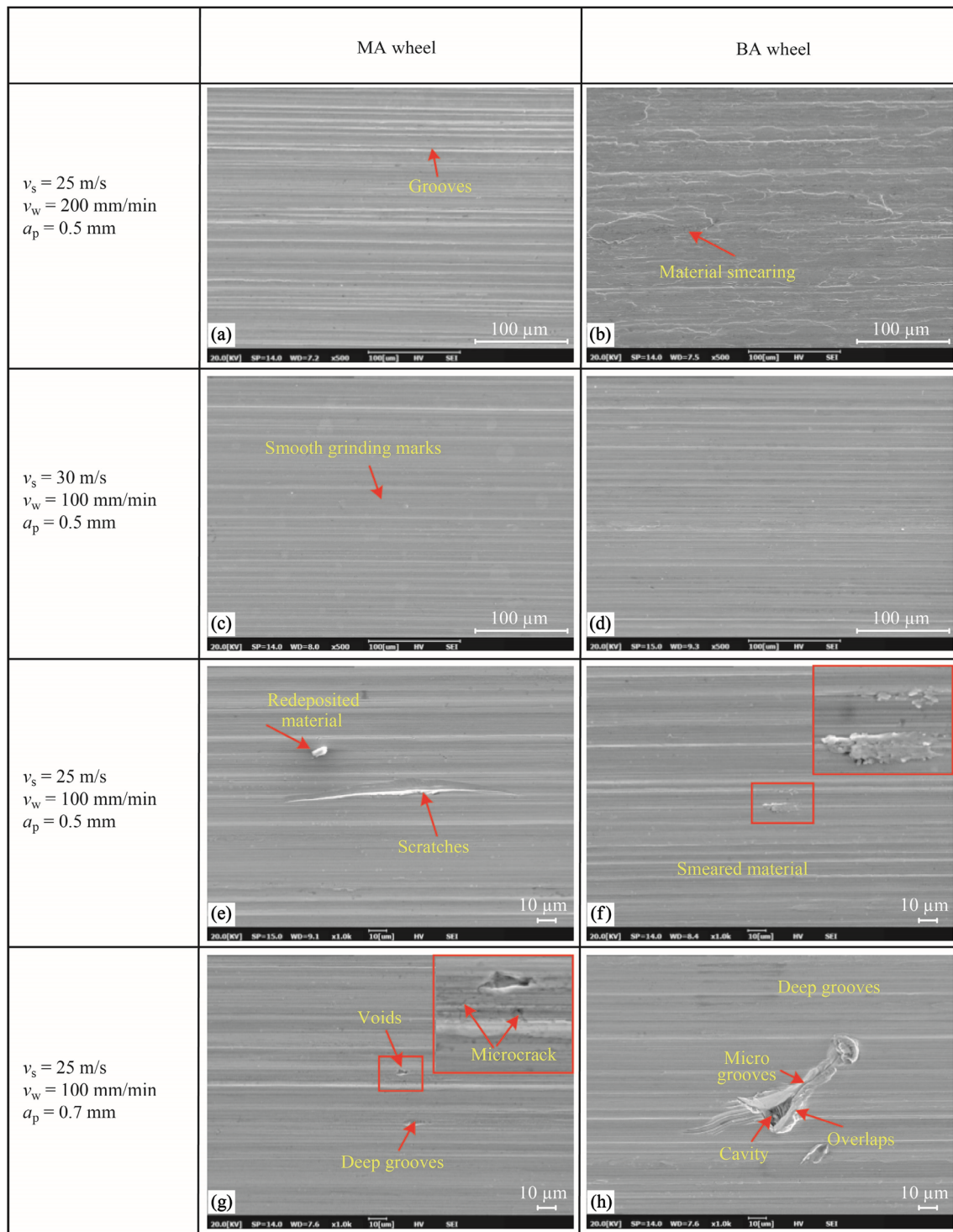


Fig. 8 Typical surface topography: the normal surface **a**, **c** and **d** and the burn surface **b** and surface defects of ground surface: **e** scratches, **f** material smeared, **g** voids and microcrack and **h** deep grooves

observed in Figs. 11a, b; the chip topography is shown in Fig. 11g. An abrasive wheel with a high porosity is generally selected to store the chips and the coolant when grinding nickel-based superalloys [44]. However, when the pores become filled with a large amount of chips, the

porosity of the abrasive wheel surface decreases, which can lead to a significant decrease in the grinding ability of the abrasive wheel and aggravate the abrasive wheel wear. Thus, it can be inferred that both the BA and MA abrasive wheels produce severe tool wear when grinding the FG96

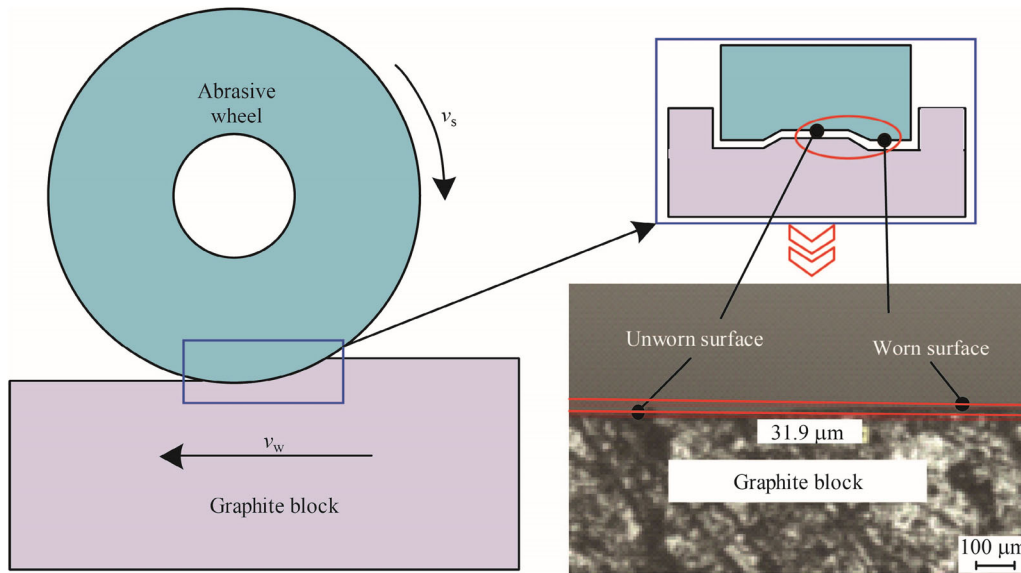


Fig. 9 Abrasive wheel wear measurement diagram

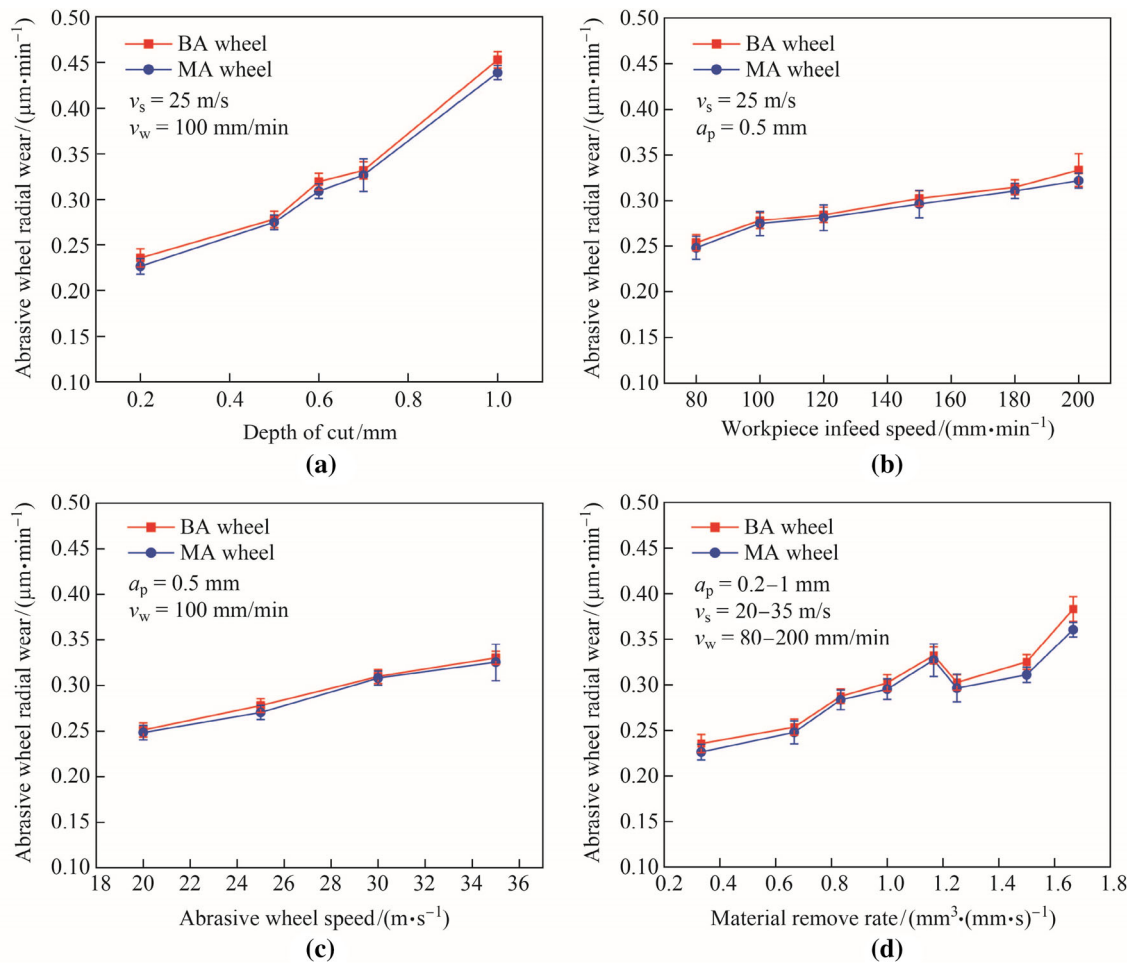


Fig. 10 Effects of **a** depth of cut, **b** workpiece infeed speed, **c** abrasive wheel speed and **d** material remove rate on abrasive wheel radial wear

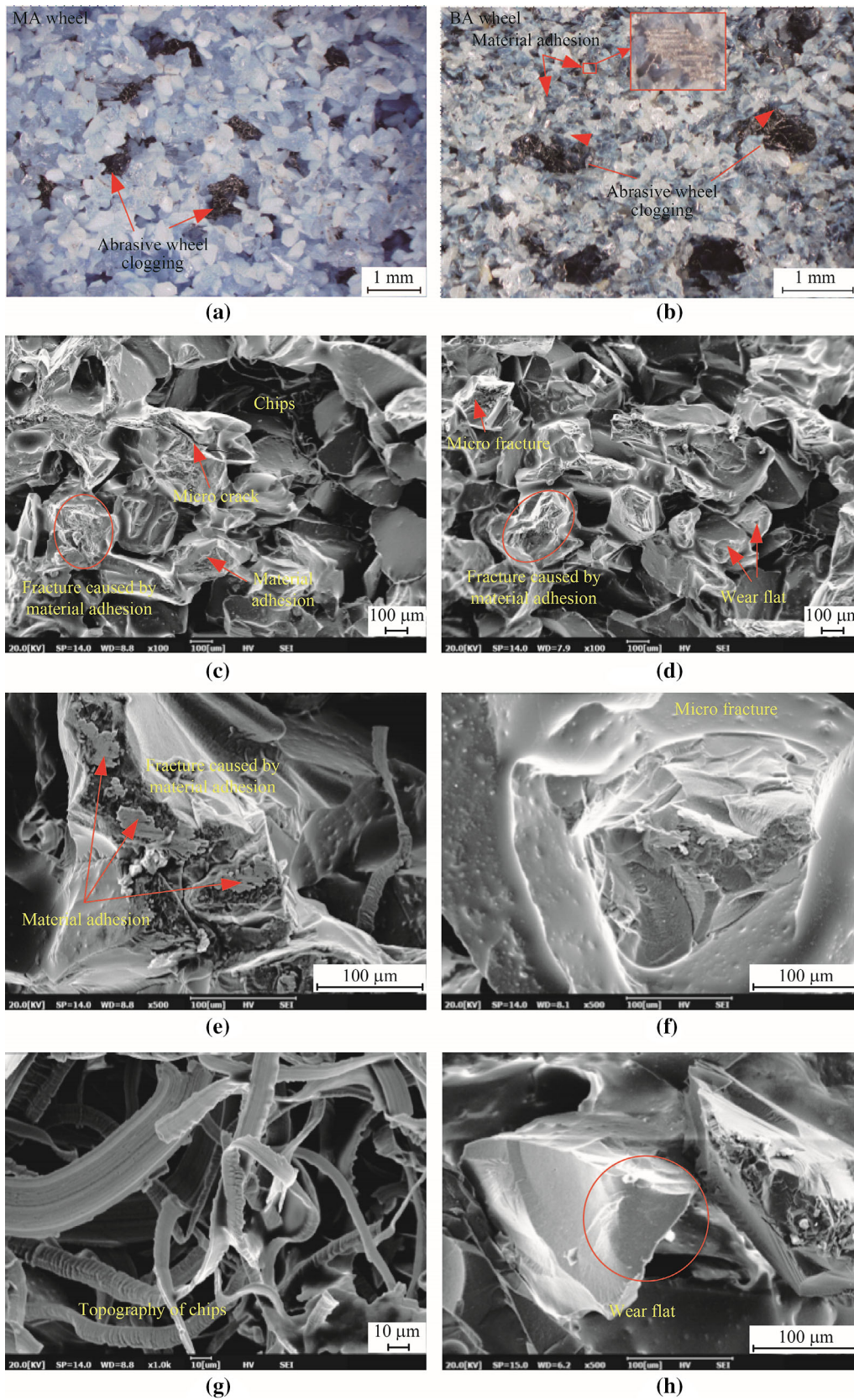


Fig. 11 Wear topographies of **a, c, e** and **g** BA abrasive wheel and **b, d, f, h** MA abrasive wheel

material. In addition, in Figs. 11c, d, it is observed that a large number of abrasive grain particles have broken due to the adhesion of the workpiece material, and micro-cracks and wear flats are also observed, as shown in Figs. 11d, f, h. This means that the main wear pattern of the two abrasive wheels during the grinding of the FGH96 material is abrasive grain fracture and attritious wear.

However, compared with the BA abrasive wheel, more micro-cracks are observed on the cutting edges of the abrasive grains on the MA abrasive wheel. Previous research has shown that micro-cracks on the cutting edge of the abrasive grains of the MA abrasive wheel might be favorable for its self-sharpening property [45]. This means that when the MA abrasive grains break along the micro-cracks, additional cutting edges will be exposed, resulting in more cutting edges actually participating in the grinding. This process is beneficial for removing the material more efficiently and reducing the grinding force [46]. In addition, the toughness and hardness of the MA abrasive wheel are higher than those of the BA abrasive wheel, which promotes wear resistance of the MA abrasive wheel during the grinding process. Thus, the wear amount of the MA abrasive wheel is lower than that of the BA abrasive wheel, as shown in Fig. 9. This is also the reason why the MA abrasive wheel achieves a higher material removal rate without surface burning than the BA abrasive wheel, as shown in Figs. 4a, b.

3.5 Grinding ratio analysis

The abrasive wheel wear is affected by a large number of factors, such as the cooling conditions, abrasive wheel characteristics, and grinding parameters. Therefore, it is difficult to analyze the abrasive wheel wear quantitatively. However, the wear resistance of the abrasive wheel can be quantitatively evaluated by the grinding ratio. Through experimental studies of friction and wear, researchers have found that the wear volume of abrasive particles can be expressed as [47–49]

$$V_{\text{grain}} = \alpha \frac{P_N^{9/8}}{K_c^{1/2} H^{5/8}} \left(\frac{E}{H}\right)^{4/5} l, \quad (2)$$

where V_{grain} is the wear volume of abrasive particles, α a constant independent of the material, P_N the normal load, K_c the fracture toughness of the abrasive particles, H the hardness of the abrasive particles, E the elastic modulus of the abrasive particles, and l the friction length of the abrasive particles.

From Eq. (2), it can be found that the wear of abrasive particles is related to the load and friction length. Therefore, it can be obtained by an analogy method considering that the abrasive wheel wear during the grinding process is

related to the grinding forces (including the tangential force (F_t) and normal grinding force (F_n)), abrasive wheel characteristics, and grinding length. In addition, the grinding width is also an important factor for the volume of abrasive wheel wear. Thus, the wear volume of the abrasive wheel (V_{wheel}) can be expressed as a function of the above three parameters,

$$V_{\text{wheel}} = k F_n^x F_t^y l'_c b_s, \quad (3)$$

where k a constant related to the characteristics of the abrasive wheel, l'_c the grinding length and b_s the grinding width. In addition, the normal and tangential grinding forces can be expressed as functions of the grinding dosage (abrasive wheel speed (m/s), workpiece infeed speed (mm/min), and depth of cut (mm)), that is

$$F_n = f(a_p, v_w, v_s) = K_1 a_p^n v_w^{n_2} v_s^{n_3}, \quad (4)$$

$$F_t = g(a_p, v_w, v_s) = K_2 a_p^m v_w^{m_2} v_s^{m_3}, \quad (5)$$

where K_1 and K_2 are constants. According to Eqs. (3)–(5), the wear volume of the abrasive wheel during the grinding process can be expressed as

$$V_{\text{wheel}} = \lambda a_p^n v_w^m v_s^z l'_c b_s. \quad (6)$$

The model for the grinding ratio, G , during the grinding process is shown in Eq. (7)

$$G = \frac{V_{\text{material}}}{V_{\text{wheel}}} = \frac{a_p l'_c b_w}{\lambda a_p^n v_w^m v_s^z l'_c b_s} = \frac{b_w}{\lambda b_s} a_p^{1-n} v_w^{-m} v_s^{-z}. \quad (7)$$

The established process for Eq. (7) can provide a new concept for model building, which is convenient for rapid prediction. According to Eq. (7), the grinding ratio of the abrasive wheel can be predicted, and thus it can be used to clarify the grinding performance of the abrasive wheel as well as to optimize the grinding parameters. For any grinding conditions, the values of λ , n , m , and z can be obtained through preliminary experiments.

According to Eq. (6), four groups of grinding parameters ($a_p = 0.5$ mm, $v_w = 100$ mm/min, and $v_s = 25$ m/s; $a_p = 1$ mm, $v_w = 100$ mm/min, and $v_s = 25$ m/s; $a_p = 0.5$ mm, $v_w = 200$ mm/min, and $v_s = 25$ m/s; $a_p = 0.5$ mm, $v_w = 100$ mm/min, and $v_s = 30$ m/s) were selected to compute the values of λ , n , m , and z under the current machined conditions. Then, the relationship between the wear volume (mm^3) of the abrasive wheels and the grinding parameters, grinding length, and grinding width of the abrasive wheel were obtained, as follows

$$V_{\text{BA}} = 0.00293 a_p^{0.70} v_w^{0.21} v_s^{0.51} l'_c b_s, \quad (8)$$

$$V_{\text{MA}} = 0.00306 a_p^{0.65} v_w^{0.21} v_s^{0.50} l'_c b_s. \quad (9)$$

The grinding ratio, G , of the two types of abrasive wheels can be obtained from Eqs. (7)–(9), as shown in

Table 4 Experimental and predicted grinding ratios G of MA and BA abrasive wheel

a_p /mm	v_w /(mm·min ⁻¹)	v_s /(m·s ⁻¹)	G ratio of MA abrasive wheel			G ratio of BA abrasive wheel		
			Experimental	Predicted	Error/%	Experimental	Predicted	Error/%
0.2	100	25	0.70	1.05	50	0.68	1.08	58.8
0.6	100	25	1.54	1.55	0.65	1.49	1.51	1.34
0.7	100	25	1.70	1.64	3.53	1.68	1.58	5.95
1	100	25	1.81	1.86	2.76	1.76	1.76	0
0.5	80	25	1.56	1.53	1.92	1.57	1.50	4.46
0.5	120	25	1.41	1.40	0.71	1.40	1.37	2.14
0.5	150	25	1.34	1.34	0	1.32	1.31	0.76
0.5	180	25	1.28	1.29	0.78	1.26	1.26	0
0.5	100	20	1.60	1.63	1.88	1.58	1.60	1.27
0.5	100	35	1.22	1.23	0.82	1.21	1.20	0.83

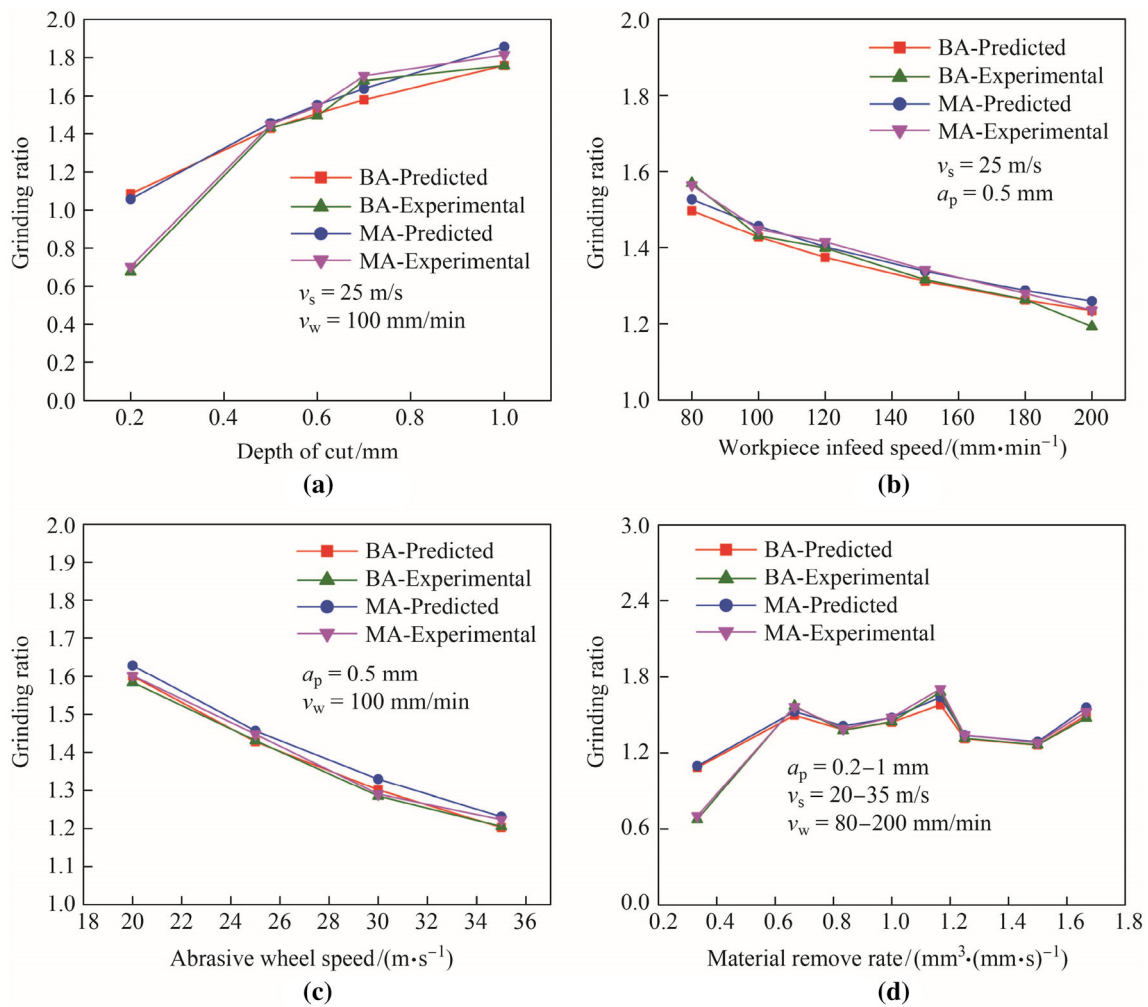


Fig. 12 Predicted and experimental grinding ratio of **a** depth of cut, **b** workpiece infeed speed, **c**) abrasive wheel speed and **d** material remove rate

Eqs. (10) and (11) for the BA and MA abrasive wheels, respectively. The predicted and experimental grinding ratios, G , of the two types of abrasive wheels with other grinding parameters are listed in Table 4. In addition, the overall results are shown in Fig. 12. From Table 4, the average relative errors in Eqs. (10) and (11) are 7.56% and 6.31%, respectively. The experimental results show that the grinding ratio of the MA abrasive wheel is larger than that of the BA abrasive wheel. Furthermore, the wear resistance of the MA abrasive wheel is superior to that of the BA abrasive wheel. Thus, the grinding performance of the MA abrasive wheel is slightly better than that of the BA abrasive wheel from the point of view of abrasive wheel wear,

$$G_{BA} = 342.5a_p^{0.30}v_w^{-0.21}v_s^{-0.51}, \quad (10)$$

$$G_{MA} = 326.8a_p^{0.35}v_w^{-0.21}v_s^{-0.50}. \quad (11)$$

It has been reported that compared with the BA abrasive wheel, the MA abrasive wheel has a much better grinding performance [44, 50]. However, the advantages of the MA abrasive wheel in grinding the FGH96 material are not significant from the perspective of the grinding force, temperature, abrasive wheel wear, and machined surface quality. This is mainly because the excellent grinding performance advantage of the MA abrasive wheel is not highlighted in this case because the two types of abrasive wheels are severely worn in the grinding process of the difficult-to-cut FGH96 material, as shown in Fig. 11.

It can be seen that the grinding ratio of powder metallurgy superalloy FGH96 is less than 1.8, as shown in Fig. 12. However, the grinding ratio is much larger when the alumina abrasive wheel is used to grind ordinary metal materials. For example, the grinding ratio in wet grinding of 100Cr6 steel using the MA abrasive wheel is from 90 to 120, as reported by Nadolny [51], while the grinding ratio of ductile iron using the BA abrasive wheel is 19 according to Shen et al. [52], and the grinding ratios of EN24 steel and casting iron are 23 and 20, respectively, using the same BA abrasive wheel according to Kalita et al. [53]. From the point of view of the grinding ratio, it is shown that the abrasive wheel wear is more severe during grinding of the FGH96 material regardless of whether the MA abrasive wheel or BA abrasive wheel is used. Thus, there is no significant difference between the two types of abrasive wheels in terms of the grinding characteristics and machined surface quality.

4 Conclusions

This study conducted an experimental investigation on the creep feed grinding of FGH96 material using MA and BA abrasive wheels. The workpiece surface quality and

grinding characteristics were estimated comparatively. The conclusions are as follows.

- (i) Under the current grinding conditions, the BA and MA abrasive wheels did not show significant differences in terms of the grinding characteristics and machined surface quality. This was mainly because the grinding advantages of the MA abrasive wheel were weakened for the difficult-to-cut FGH96 material.
- (ii) Serious tool wear occurred with both the MA and BA abrasive wheels as wheel clogging and workpiece material adhesion took place during the grinding of FGH96, which had adverse effects on the machined surface quality.
- (iii) A prediction model for the grinding ratio was established with acceptable errors of 7.56% and 6.31% for the BA and MA abrasive wheels, respectively, during the current creep-feed deep grinding of FGH96. The predicted results showed good agreement with the experimental results (ranging from 0.6 to 1.8).

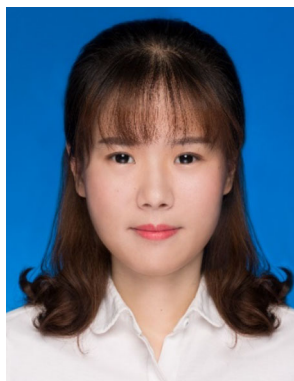
Acknowledgements This work was financially supported by the National Natural Science Foundation of China (Grant Nos. 51775275 and 51921003), National Major Science and Technology Project (Grant No. 2017-VII-0002-0095), Funding for Outstanding Doctoral Dissertation in NUAA (Grant No. BCXJ19-06), the Six Talents Summit Project in Jiangsu Province (Grant No. JXQC-002) and Fundamental Research Funds for the Central Universities (Grant No. NP2018110).

References

1. Peng Z, Tian G, Jiang J et al (2016) Mechanistic behaviour and modelling of creep in powder metallurgy FGH96 nickel superalloy. *Mater Sci Eng A* 676:441–449
2. Devillez A, Le Coz G, Dominiak S et al (2011) Dry machining of Inconel 718 workpiece surface integrity. *J Mater Process Technol* 211:1590–1598
3. Daddona DM, Raykar SJ, Narke MM (2017) High speed machining of Inconel 718: tool wear and surface roughness analysis. *Procedia CIRP* 62:269–274
4. Du J, Liu ZQ (2013) Damage of the machined surface and subsurface in orthogonal milling of FGH95 superalloy. *Int J Adv Manuf Technol* 68:1573–1581
5. Du J, Liu ZQ, Yi W et al (2011) Influence of cutting speed on surface integrity for powder metallurgy nickel-based superalloy FGH95. *Int J Adv Manuf Technol* 56:553–559
6. Du J, Liu ZQ (2012) Effect of cutting speed on surface integrity and chip morphology in high-speed machining of PM nickel-based superalloy FGH95. *Int J Adv Manuf Technol* 60:893–899
7. Zhou JM, Bushlya V, Stahl JE (2012) An investigation of surface damage in the high speed turning of Inconel 718 with use of whisker reinforced ceramic tools. *J Mater Process Technol* 212:372–384

8. Sugihara T, Takemura S, Enomoto T (2016) Study on high-speed machining of Inconel 718 focusing on tool surface topography of CBN cutting tool. *Int J Adv Manuf Technol* 87:9–17
9. Thakur A, Gangopadhyay S (2016) State-of-the-art in surface integrity in machining of nickel-based super alloys. *Int J Mach Tools Manuf* 100:25–54
10. Miao Q, Li HN, Ding WF (2020) On the temperature field in the creep feed grinding of turbine blade root: simulation and experiments. *Int J Heat Mass Transf* 147:118957
11. Ulutan D, Ozel T (2011) Machining induced surface integrity in titanium and nickel alloys: a review. *Int J Mach Tools Manuf* 51:250–280
12. Linke BS (2015) Review on grinding tool wear with regard to sustainability. *J Manuf Sci Eng Trans ASME* 137:060801
13. Zhou YG, Gong Y, Zhu Z et al (2016) Modelling and optimization of surface roughness from micro-grinding of nickel-based single crystal superalloy using the response surface methodology and genetic algorithm. *Int J Adv Manuf Technol* 85:2607–2622
14. Żyłka Ł, Płodzień M, Babiarczyk R (2018) The influence of grinding speed on the creep-feed grinding process. *J Mech Energy Eng* 2:285–290
15. Zeng Q, Liu G, Liu L et al (2015) Investigation into grindability of a superalloy and effects of grinding parameters on its surface integrity. *Proc Inst Mech Eng Part B J Eng Manuf* 229:238–250
16. Miao Q, Ding WF, Gu YL et al (2019) Comparative investigation on wear behavior of brown alumina and microcrystalline alumina abrasive wheels during creep feed grinding of different nickel-based superalloys. *Wear* 426/427:1624–1634
17. Li M, Ding WF, Li BK et al (2019) Morphological evolution and grinding performance of vitrified bonded microcrystal alumina abrasive wheel dressed with a single-grit diamond. *Ceram Int* 45:19669–19678
18. Qian N, Ding WF, Zhu YJ (2018) Comparative investigation on grindability of K4125 and Inconel718 nickel-based superalloys. *Int J Adv Manuf Technol* 97:1649–1661
19. Yao CF, Jin QC, Huang XC et al (2013) Research on surface integrity of grinding Inconel718. *Int J Adv Manuf Technol* 65:1019–1030
20. Wang YG, Li CH, Zhang YB et al (2016) Experimental evaluation of the lubrication properties of the wheel/workpiece interface in MQL grinding with different nanofluids. *Tribol Int* 99:198–210
21. Xu XP, Yu YQ, Xu HJ (2002) Effect of grinding temperatures on the surface integrity of a nickel-based superalloy. *J Mater Process Technol* 129:359–363
22. Sinha MK, Setti D, Ghosh S et al (2016) An investigation on surface burn during grinding of Inconel 718. *J Manuf Processes* 21:124–133
23. Naskar A, Singh BB, Choudhary A et al (2018) Effect of different grinding fluids applied in minimum quantity cooling-lubrication mode on surface integrity in cBN grinding of Inconel 718. *J Manuf Processes* 36:44–50
24. Ding WF, Xu JH, Chen ZZ et al (2010) Grindability and surface integrity of cast nickel-based superalloy in creep feed grinding with brazed CBN abrasive wheels. *Chin J Aeronaut* 23:501–510
25. Nadolny K (2014) State of the art in production, properties and applications of the microcrystalline sintered corundum abrasive grains. *Int J Adv Manuf Technol* 74:1445–1457
26. Miao Q, Ding WF, Kuang WJ et al (2020) Comparison on grindability and surface integrity in creep feed grinding of GH4169, K403, DZ408 and DD6 nickel-based superalloys. *J Manuf Processes* 49:175–186
27. Yu TY, Asplund DT, Bastawros AF et al (2016) Performance and modeling of paired polishing process. *Int J Mach Tools Manuf* 109:49–57
28. Li HN, Yu TB, Wang ZX et al (2017) Detailed modeling of cutting forces in grinding process considering variable stages of grain-workpiece micro interactions. *Int J Mech Sci* 126:319–339
29. Li Z, Ding WF, Shen L et al (2016) Comparative investigation on high-speed grinding of TiCp/Ti-6Al-4V particulate reinforced titanium matrix composites with single-layer electroplated and brazed CBN wheels. *Chin J Aeronaut* 29:1414–1424
30. Shi XL, Xiu SC, Su HL (2019) Residual stress model of pre-stressed dry grinding considering coupling of thermal, stress, and phase transformation. *Adv Manuf* 7:401–410
31. Dai SJ, Li XQ, Zhang HB (2019) Research on temperature field of non-uniform heat source model in surface grinding by cup wheel. *Adv Manuf* 7(3):326–342
32. Ding WF, Zhang L, Li Z et al (2017) Review on grinding-induced residual stresses in metallic materials. *Int J Adv Manuf Technol* 88:2939–2968
33. Maksud TMA (2005) Heat transfer model for creep-feed grinding. *J Mater Process Technol* 168:448–463
34. Dai CW, Ding WF, Zhu YJ et al (2018) Grinding temperature and power consumption in high speed grinding of Inconel 718 nickel-based superalloy with a vitrified CBN wheel. *Precis Eng* 52:192–200
35. Gu YL, Li HN, Du BC et al (2019) Towards the understanding of creep-feed deep grinding of DD6 nickel-based single-crystal superalloy. *Int J Adv Manuf Technol* 100:445–455
36. Li Z, Ding WF, Liu CJ et al (2018) Grinding performance and surface integrity of particulate-reinforced titanium matrix composites in creep-feed grinding. *Int J Adv Manuf Technol* 94:3917–3928
37. Rowe WB (2001) Thermal analysis of high efficiency deep grinding. *Int J Mach Tools Manuf* 41:1–19
38. Hecker RL, Liang SY (2013) Predictive modeling of surface roughness in grinding. *Int J Mach Tools Manuf* 43:755–761
39. Wu WT, Li CH, Yang M et al (2019) Specific energy and g ratio of grinding cemented carbide under different cooling and lubrication conditions. *Int J Adv Manuf Technol* 105(1/4):67–82
40. Gao T, Li CH, Zhang YB et al (2019) Dispersing mechanism and tribological performance of vegetable oil-based CNT nanofluids with different surfactants. *Tribol Int* 131:51–63
41. Zhou W, Peng K, Yu Y (2016) Surface roughness measurement and analysis of mechanical parts based on digital holography. *Adv Manuf* 4(3):217–224
42. Kovach JA, Malkin S (1988) Thermally induced grinding damage in superalloy materials. *CIRP Ann* 37:309–313
43. Fredj NB, Sidhom H, Braham C (2006) Ground surface improvement of the austenitic stainless steel AISI 304 using cryogenic cooling. *Surf Coat Technol* 200:4846–4860
44. Rowe WB (2009) Principles of modern grinding technology. Elsevier, Amsterdam, pp 82–87
45. Miao Q, Ding WF, Kuang WJ et al (2020) Tool wear of vitrified microcrystalline alumina wheels in creep feed profile grinding of turbine blade root of single crystal nickel-based superalloy. *Tribol Int* 145:106144
46. Dai CW, Ding WF, Xu JH et al (2017) Influence of grain wear on material removal behavior during grinding nickel-based superalloy with a single diamond grain. *Int J Mach Tools Manuf* 113:49–58
47. Malkin S, Hwang TW (1996) Grinding mechanisms for ceramics. *CIRP Ann Manuf Technol* 45(1996):569–580
48. Doğan CP, Hawk JA (2001) Microstructure and abrasive wear in silicon nitride ceramics. *Wear* 250:256–263
49. Miyazaki H, Hyuga H, Yoshizawa YI et al (2009) Correlation of wear behavior and indentation fracture resistance in silicon nitride ceramics hot-pressed with alumina and yttria. *J Eur Ceram Soc* 29:1535–1542

50. Godino L, Pombo I, Sanchez JA et al (2018) On the development and evolution of wear flats in microcrystalline sintered alumina grinding wheels. *J Manuf Processes* 32:494–505
51. Nadolny K (2015) Wear phenomena of grinding wheels with sol-gel alumina abrasive grains and glass-ceramic vitrified bond during internal cylindrical traverse grinding of 100Cr6 steel. *Int J Adv Manuf Technol* 77:83–98
52. Shen B, Malshe AP, Kalita P et al (2008) Performance of novel MoS₂ nanoparticles based grinding fluids in minimum quantity lubrication grinding. *Trans NAMRI/SME* 36(357):e364
53. Kalita P, Malshe AP, Kumar SA et al (2012) Study of specific energy and friction coefficient in minimum quantity lubrication grinding using oil-based nanolubricants. *J Manuf Processes* 14:160–166



Min Li is currently a Ph.D. candidate of Mechanical Engineering at Nanjing University of Aeronautics and Astronautics, People's Republic of China. Her research interest is dressing technology of alumina abrasive tools.



Ben-Kai Li is currently a Ph.D. candidate of Mechanical Engineering at Nanjing University of Aeronautics and Astronautics, People's Republic of China. His research interest is grinding technology of difficult-to-cut materials.



Xi Zhang is currently a Master student of Mechanical Engineering at Nanjing University of Aeronautics and Astronautics, People's Republic of China. His research interest is grinding technology of difficult-to-cut materials.



Qing Miao is currently a Ph.D. candidate of Mechanical Engineering at Nanjing University of Aeronautics and Astronautics, People's Republic of China. His research interest is grinding technology of difficult-to-cut materials.



Wen-Feng Ding is currently a Professor of Mechanical Engineering and Doctoral Supervisor at Nanjing University of Aeronautics and Astronautics, People's Republic of China. His research interests include grinding technology and equipment, superhard abrasive tools, machining process simulation and control technology.